

# Seismic detection and analysis of icequakes at Columbia Glacier, Alaska

Shad O'Neel,<sup>1</sup> H. P. Marshall,<sup>1</sup> D. E. McNamara,<sup>1</sup> and W. T. Pfeffer<sup>1</sup>

Received 13 June 2006; revised 2 October 2006; accepted 6 November 2006; published 3 May 2007.

[1] Contributions to sea level rise from rapidly retreating marine-terminating glaciers are large and increasing. Strong increases in iceberg calving occur during retreat, which allows mass transfer to the ocean at a much higher rate than possible through surface melt alone. To study this process, we deployed an 11-sensor passive seismic network at Columbia Glacier, Alaska, during 2004–2005. We show that calving events generate narrow-band seismic signals, allowing frequency domain detections. Detection parameters were determined using direct observations of calving and validated using three statistical methods and hypocenter locations. The 1–3 Hz detections provide a good measure of the temporal distribution and size of calving events. Possible source mechanisms for the unique waveforms are discussed, and we analyze potential forcings for the observed seismicity.

**Citation:** O'Neel, S., H. P. Marshall, D. E. McNamara, and W. T. Pfeffer (2007), Seismic detection and analysis of icequakes at Columbia Glacier, Alaska, *J. Geophys. Res.*, 112, F03S23, doi:10.1029/2006JF000595.

## 1. Introduction

[2] Retreating marine-terminating glaciers play a significant role in global sea level rise because channelized discharge culminating in iceberg calving allows mass transfer from the glacier to the ocean much faster than possible by surface melt alone. For example, at rapidly retreating LeConte Glacier, *Motyka et al.* [2003] estimate that calving losses are on the order of 15 times those due to surface ablation. Rapid calving retreats are currently occurring in both Alaska and Greenland, heightening the importance of understanding such processes [e.g., *Krabill et al.*, 2004; *Howat et al.*, 2005; *O'Neel et al.*, 2005; *Rignot and Kanagaratnam*, 2006; *Ekström et al.*, 2006; *Joughin*, 2006; *Arendt et al.*, 2006]. Many similarities in dynamics exist between Greenland outlet glaciers and Alaskan tidewater glaciers, which are the source of today's predominant contribution to sea level rise [*Rignot and Kanagaratnam*, 2006; *Dyurgerov and McCabe*, 2006]. However, quantitative measurement methods and a predictive capacity for calving are hampered by our inability to record and interpret calving events remotely, and our poor understanding of the physics of calving.

[3] Several studies have shown that glaciers can generate seismic signals called icequakes [e.g., *Neave and Savage*, 1970; *Van Wormer and Berg*, 1973; *Weaver and Malone*, 1979; *Wolf and Davies*, 1986; *Qamar*, 1988; *Anandakrishnan and Bentley*, 1993], but most of these studies focused on terrestrial glaciers and some of the earlier studies were affected by instrument limitations. Recently, work by *Ekström et al.* [2003, 2006] has shown

that large energetic events (earthquake magnitude  $\sim 4$ –5) recorded on global networks at long periods (35–150 s) are associated with outlet glaciers in Greenland, with possible source mechanisms including rapid basal sliding or calving [*Joughin*, 2006]. Pioneering work by *Qamar* [1988] at Columbia Glacier established that calving events generate seismic signals with different characteristics than seismograms generated by earthquakes or crevassing, which is the predominant signal recorded on land terminating glaciers [*Neave and Savage*, 1970].

[4] Seismograms of calving events are typically emergent, long-lived (2–1000 s) and dominated by lower frequencies (1–3 Hz) [*Wolf and Davies*, 1986; *Qamar*, 1988], while crevassing events are characterized by impulsive onsets, short durations (0.1–1 s) and a high characteristic frequency  $\sim 100$  Hz [*Neave and Savage*, 1970]. Signals originating near the bed have been assumed to result from stick-slip motion [*Weaver and Malone*, 1979], and *Deichmann et al.* [2000] showed that basal events lack surface waves that are present in near-surface crevassing signals. Some of these signals may be related to changes in the subglacial hydraulic system [e.g., *St. Lawrence and Qamar*, 1979].

[5] In this paper, we outline techniques to use passive seismology to remotely monitor and automatically detect icequakes generated by Columbia Glacier. Similar to *Qamar* [1988], we associate events in the 1–3 Hz frequency band with calving and confirm this using direct observations. Then by exploiting the unique spectral signatures of different styles of icequakes, using methods taken from seismology, photogrammetry and statistics, we show it is possible to detect and separate icequakes by their physical process of origination. After method validation, we discuss possible underlying reasons for the distinct waveform characteristics associated with calving. We make a brief analysis of temporal patterns for calving and possible forcing mecha-

<sup>1</sup>Institute of Arctic and Alpine Research, University of Colorado, Boulder, Colorado, USA.

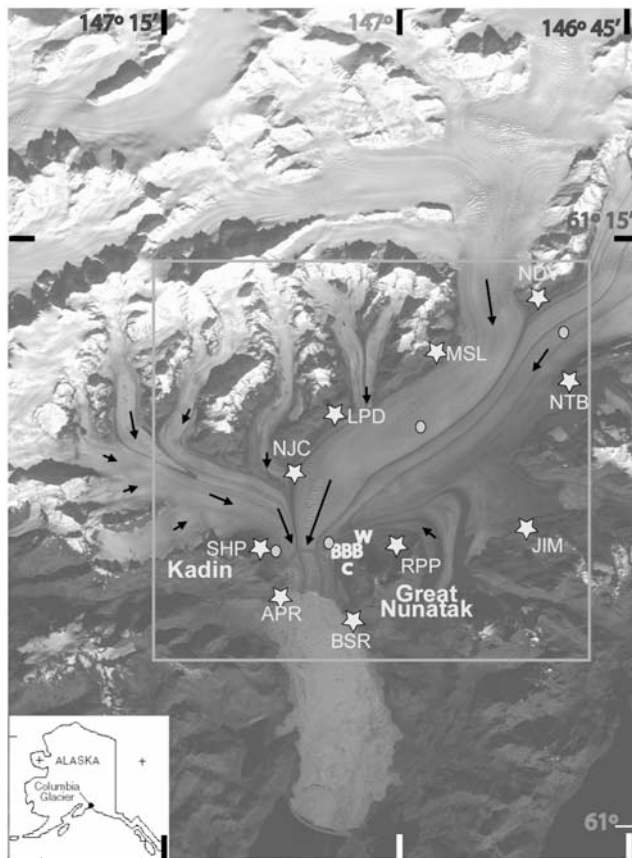


**Figure 1.** Lower Columbia Glacier as imaged by Landsat thematic Mapper on 26 September 1999. Black arrows give nominal flow directions and relative speeds. Stars mark the location of high-frequency seismic stations, and BBB marks the location of the broadband seismometer. Station codes are shown for each seismometer. W shows the location of the weather observations, and the C marks the time-lapse camera. Circles show approximate locations of blasting sites. The 2004–2005 terminus position is roughly shown as a line upstream of the 1999 terminus. The preretreat terminus position is shown at the downstream edge of the fjord. The approximately  $20 \times 20$  km box outlines the region shown in Figure 9 to facilitate comparison.

nisms. This new detection method offers great potential to enhance our knowledge of marine terminating glacier retreat, and provides a crucial step toward a direct measurement for iceberg calving.

## 2. Field Area

[6] Columbia Glacier is a temperate, tidewater glacier located in the Chugach Mountains of south central Alaska, about 30 km west of Valdez (Figure 1). This large tidewater glacier attained a stable, extended geometry with a length exceeding 66 km and area of  $\sim 1100$  km<sup>2</sup> around 1100 A.D. [Calkin *et al.*, 2001]. Columbia Glacier is at the melting point throughout the entire glacier, and is grounded along its full 52 km length. A rapid retreat began around 1980, and since then the glacier has lost approximately 75 km<sup>2</sup> of area and has thinned by nearly 400 m (roughly 35%) at the location of the present terminus. Volume changes from

Columbia Glacier are among the most significant in Alaska; this single glacier contributed  $\sim 50\%$  of the volume loss from the Chugach Mountains during the last 50 years [Arendt *et al.*, 2006].

[7] The current water depth at the terminus is approximately 500 m. Any stability provided by the submarine terminal moraine [Fischer and Powell, 1998] was lost soon after the initiation of retreat when the terminus entered deep water. Shortly after the retreat began, ice velocities and along-flow strain rates increased and have continued to do so until very recently. Photogrammetrically determined speeds have exceeded  $25 \text{ m d}^{-1}$  with associated extensional strain rates  $>2.2 \text{ yr}^{-1}$  and estimated ice fluxes in excess of  $6.5 \text{ km}^3 \text{ yr}^{-1}$  [Krimmel, 2001; O'Neel *et al.*, 2005]. However, recent near-terminus velocity measurements document a 40–50% slowdown. Because variability in these fields has increased over time, and because the current terminus is located in the region of recently abandoned maximum basal drag [O'Neel *et al.*, 2005], we believe this slowdown is temporary and does not indicate the termination of the retreat.

## 3. Methods

[8] A variety of field data are used in this study, including passive seismic observations, terrestrial time-lapse photographs, weather data, and a qualitative observational record of calving events, modeled closely after the observations published by O'Neel *et al.* [2003] at LeConte Glacier. Using our field observations, we have designed, optimized and validated a new seismic detector. This method is able to isolate calving from other seismic events, providing a new investigative technique for the study of marine terminating glacier dynamics.

### 3.1. Passive Seismology

[9] An array of 11 seismometers was deployed around the lower 20 km of the glacier for a period of 12 months (Figure 1). Ten of the instruments were high-frequency, three-axis seismometers (Mark L22; peak response at 2 Hz) and one instrument was a broadband sensor (Guralp 40T; flat response from 30 s to 100 Hz). Rapid motion, ablation, and intense fracturing prohibited instrument installation on the glacier surface, thus all seismometers were deployed on bedrock positions surrounding the lower glacier (Figure 1). During this period, we performed 2 service runs and spent a total of 7 weeks making visual observations at the glacier terminus. Seismometers recorded continuously at a sampling frequency of 100 Hz, logging over 60 GB of data to Reftek RT130 digitizers during 238 days of active recording throughout the deployment. Large data gaps occur (especially during winter) due to memory limitations, power failures, and equipment malfunctions. Here we focus on data from the broadband instrument, which remained in operation for an additional three months after the main array was removed, but use other stations in hypocenter solutions.

### 3.2. Time-Lapse Photography

[10] An 8 M pixel digital camera was mounted to a steep cliff face with full view of the terminus and programmed to take four pictures daily. The location of

the camera and 2 control points were surveyed to  $\sim 5$  cm precision using GPS. Camera pointing angles were measured at the time of installation and during each service run. The camera was installed during June 2004 and operated until 29 December 2004. Data gaps due to camera malfunction in cold weather exist near the end of the record, when the camera functioned only on sunny days.

### 3.3. Weather Data

[11] A Campbell Scientific weather station installed near the broadband seismometer, recorded air temperature and relative humidity over the entire duration of the study. We obtained 6 hr precipitation data collected in Valdez by NOAA (station PAVW <http://gis.ncdc.noaa.gov>). The relationship between precipitation at Columbia Glacier and Valdez is unknown, but temperatures at the two sites show a high level of correlation ( $\rho = 0.75$  at 0.5 d lag).

### 3.4. Iceberg Calving Observer Record

[12] Iceberg calving at Columbia Glacier is an energetic and dramatic process. Styles of calving events are diverse, ranging from small avalanches and spalls (crushed particles to 50 m slabs) that can be acoustically loud, to very large ( $\sim 1$  km<sup>2</sup> iceberg surface area) submarine events that are often acoustically quiet. During June 2005 and, to a lesser extent, during June 2004, we made detailed observations of calving events. Observers noted times of calving event occurrences along with the location of the event, the style of each event, its magnitude and whether or not the event appeared to be associated with rapid and voluminous discharge of subglacial water.

[13] Observer documentation exists for 940 events with sequential photographs for dozens of large events. Although the open-ended measurement scale is highly subjective, the four observing researchers were able to calibrate their observations to within one level of magnitude within three days. Magnitude 1 events represent small (e.g.,  $60 \times 10 \times 1$  m) slabs breaking off the terminus. The largest witnessed event earned a magnitude 20 by failing across the entire 2.5 km width of the terminus, several hundred meters upstream. This event released several submarine bergs and filled approximately 15 km<sup>2</sup> of the forebay with ice debris within 20 min. We visually detected changes in cliff height and surface slope in the near terminus region following this event.

[14] Events were classified as either subaerial or submarine based on their detachment above or below sea level [Motyka, 1997]. Subaerial events occur with the greatest frequency, nominally tens per hour, while submarine events occur less often, with quiescent periods of several days between episodes of elevated activity (typically one to three large events on active days). Submarine melt provides a significant contribution to the calving flux, but is not separable (nor visually detectable) in any quantifiable way.

[15] Subaerial events were further separated into categories including avalanches, block slumps, column drops, and column rotations. Submarine icebergs were classified by the origination depth as shallow, deep or basal, based on the color of the iceberg [Motyka, 1997]. When observed, serac collapses upstream of the terminus were documented as internal calving events, and we recorded the times of loud

cracks, akin to gunfire, that were not associated with a visible calving event.

## 4. Analysis

### 4.1. Designing an Icequake Detector

[16] The development of a frequency domain icequake detector relied heavily on field observations and first-order analyses of seismic data associated with these observations. We describe these first-order results before presenting the development of the event detector.

#### 4.1.1. Observer Record

[17] Over 85% of calving events witnessed during our observation period occurred subaerially. Of all subaerial events, column drops dominated, comprising over 50% of all events. Infrequent submarine events composed only  $\sim 10$ –15% of observed events. Although our open-ended magnitude scale reached a maximum value of 20, the mean magnitude was  $\sim 2$ , and the highly skewed distribution indicates that large events are rare. Our observations showed that submarine bergs are always released during large volume events, but they may be triggered by subaerial events. Approximately 2% of all observed events were associated with massive release of subglacial water, and these “floods” only occurred during release of submarine bergs. An ice free forebay is a phenomenon only observed since 2004, and the thick floating ice debris (combined with more distal observation platforms) prior to this time probably prevented detection of these flood events by previous researchers.

#### 4.1.2. Seismic Data

[18] To illustrate calving events and the associated seismic data, we show a mid event photograph in Figure 2a. Twelve minutes of broadband seismic data (vertical channel) during this large submarine calving event are shown in Figure 2b. The inset gives a detailed view of the emergent onset during the first 55 s of the record.

[19] In contrast to seismic signals generated by earthquakes, we demonstrate that all calving events, regardless of size or type, have similar spectra, with the dominant power contained in the 1–3 Hz frequency band. Some events, irrespective of style or size, have a low-frequency peak in power (0.04–0.2 Hz), but this peak exceeds the 1–3 Hz peak only  $\sim 5\%$  of the time in a set of 80 observed and analyzed events. Figure 3 displays the unique spectral characteristics of these events, comparing them to tectonic earthquakes and background noise. Figure 3a shows a normalized power spectral density for a local earthquake ( $M_L = 2.8$ , 12 June 2005, 1843:47). This spectrum, with a corner frequency around 3.5 Hz is typical of a small tectonic event. Figure 3b shows the spectrum for background noise (no events). This spectrum is characterized by maximum power at 0.2 Hz in the microseism band [Stein and Wysession, 2003], primarily forced by ocean waves in the fjord. Figure 3c shows spectra for both a small and a large calving event. As determined by direct comparison of seismic waveforms recorded during observed events, both these spectra are typical of calving, with a majority of power focused in the narrow-frequency band between 1–3 Hz.

[20] Crevassing events have also been shown to have unique spectral characteristics. Although Neave and Savage [1970] found that crevassing events observed and recorded



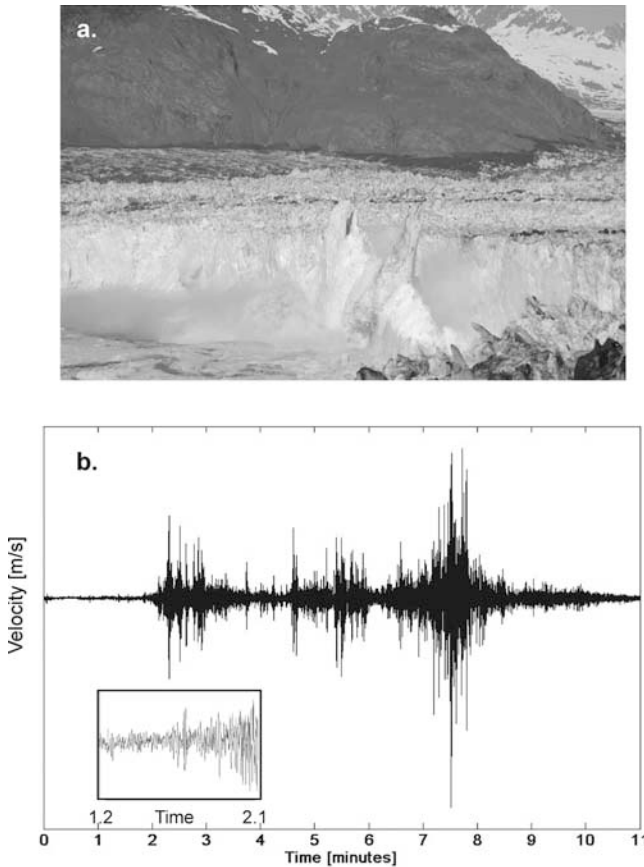


**Figure 2.** (a) Midevent photograph of a large submarine calving event that occurred between 1857 and 1910 UTC on 17 June 2005. For scale the ice cliff is approximately 70 m tall. The emerging berg was propelled approximately 10% higher than the ice cliff during release, then rotated to form a tabular slab  $\sim 300 \times 500$  m in size before disaggregating into several small pieces. (b) Twelve minutes of broadband data during this event. The inset shows 55 s of data near the event onset to highlight the emergent nature of the calving events.

at Athabasca Glacier possessed a characteristic frequency of 100 Hz, at Columbia Glacier power at frequencies in excess of 30 Hz is rare. This may be because our sampling interval of 100 Hz allows resolution only below the 50 Hz Nyquist frequency, or because warmer ice exhibits lower characteristic frequencies for similar events. The high-frequency energy associated with crevassing may also be completely attenuated upon arrival at the rock-based seismometers. This statement agrees with first-order estimates of a low seismic quality factor,  $Q$ , for ice [Métiexian *et al.*, 2003]. Regardless of the explanation, many events detected in the 10–20 Hz passband fit literature descriptions of crevassing events. We investigate the likelihood that event detections in this frequency range represent crevassing, although our main focus is on the seismic signals produced by iceberg calving.

#### 4.2. A Frequency Domain Detector

[21] Earthquake seismologists often use the ratio of seismogram short-term and long-term average amplitude (STA, LTA, respectively) to automatically detect events

[e.g., Lee and Stewart, 1981]. Given a set of window lengths, event triggers are marked and cataloged when the ratio exceeds a user-defined threshold. However, STA/LTA ratios remain small near emergent event onsets, resulting in frequent misdetections of calving generated icequakes. Because of the monochromatic nature of calving event waveforms, distinct from crevassing events and most earthquakes, we developed a frequency domain detector to automatically detect and catalog icequakes.

[22] To detect events, we calculate the frequency spectrum (PSD) for 50% overlapped subsets of data from a given station/channel. We minimize spectral leakage by using a windowed fast Fourier transform (FFT):

$$PSD(f) = \left| \int w(n)V(t)e^{if2\pi t} dt \right|^2 \quad (1)$$

where  $w(n)$  is the window function defined over the range of data points  $n = -N/2: N/2$ , for  $N$  total samples in the subset,  $V(t)$  is the recorded time domain signal, and  $f$  is frequency in Hz. After experimenting with many different window functions, we chose to follow Harris [1978] and used the Kaiser-Bessel window,

$$w(n, \alpha) = \frac{I_0 \left[ \pi \alpha \sqrt{1 - \left( \frac{2n}{N} \right)^2} \right]}{I_0(\pi \alpha)} \quad (2)$$

where  $I_0$  is the zeroth-order modified Bessel function of the first kind. This window contains a parameter  $\alpha$ , proportional to the time-bandwidth product, that can be adjusted to either minimize spectral leakage or maximize frequency resolution.

[23] A band pass filter applied to the transformed data isolates a frequency band of interest for analysis. In order to characterize the general features of the passband data, we calculate a statistic (mean, maximum, or standard deviation), of the power spectrum in each time window across the specified passband. The statistic may be normalized by the median value over the entire processing segment (1–24 hours). When the statistic passes a user defined threshold value, event detection is enabled, and when the statistic drops back below the threshold value, event detection is disabled.

[24] Detector output includes the time varying power spectral density, detection parameters (also input), start and stop times of detections and detection durations at the resolution of half the window width. The detector is written in MATLAB<sup>®</sup>, with both a graphical user interface, designed to facilitate parameter exploration, and a batch processing module to allow automated detection over an entire data set. Software can be obtained by contacting the authors.

[25] In this study, we analyze the following three bands: (1) 1–3 Hz, the frequencies over which calving energy is focused, (2) 10–20 Hz, which may capture crevassing and other fracturing, and (3) a low-frequency band ranging from 0.03 to 0.083 Hz (equivalently 15–30 s periods), which records large teleseismic events and may contain other information.

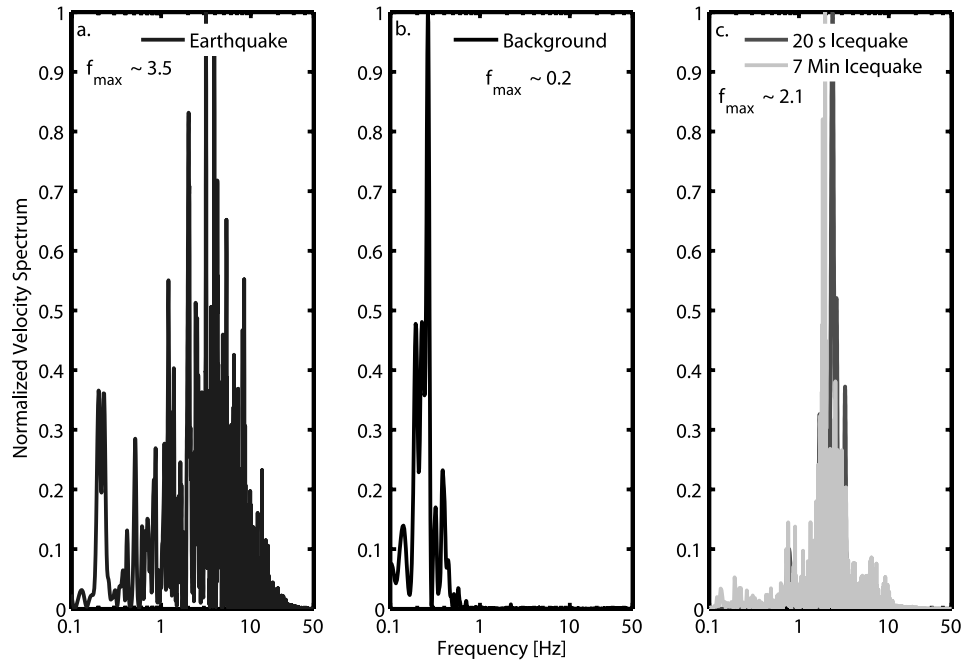


**Figure 3.** Normalized velocity PSD plots for various seismic events. (a) Local earthquake with a corner frequency at  $\sim 3.5$  Hz. (b) PSD characterized by power in the microseism band, during an event free time period. The peak frequency at 0.2 Hz is probably related to ocean waves. (c) Two calving events, which show the similar frequency content for icequakes with vastly different durations but different frequency content than either background noise or tectonic events.

#### 4.3. Detection Parameter Selection

[26] We used the observer record to choose a set of detection parameters for the 1–3 Hz passband. Parameter selection was achieved via penalty function analysis, where penalties were based on the time difference between observations and detections. If a detection was recorded within 30 s of an observation (allowing for initiation of seismic signal prior to visual detection), the assigned penalty was the square of the time difference between the observation and detection. A maximum, fixed penalty was assigned in cases where a noted observation had no associated detection. Intermediate, fixed penalties were assigned for detections lacking an observation (to allow for missed observations). Evaluation of detector performance occurred over a realistic range of a reduced parameter set (window size, statistic, normalization and threshold value), with segment duration, window shape and window overlap fixed before the search. The parameter set that achieved the minimum penalty score was selected and fixed for all passbands. Identical parameters were applied to the other passbands because we lack other observer records (e.g., crevassing, sliding) to “tune” these passbands.

[27] We selected 17 hour-long data sets of complete visual observations to obtain detection parameters. These data are well distributed through daylight hours, and span quiescent conditions (3 small events) to repeated large submarine events contained within an hour (15 events). We chose to count event detections over 1 hour data segments to avoid misdetections due to background noise variance over longer timescales. Given our chosen FFT kernel window length of 25 s, event time resolution is 12.5 s. This choice effectively

rejects the small, short-duration and low-energy events, while detecting events that contribute significantly to changes in the volume of the glacier. Short-duration events are still captured if significant energy is released, as evidenced by the high number of detections in the 10–20 Hz passband, many of which last less than 1 s (visual inspection). To better represent the calving process, we assigned 3 s durations for events with minimum resolution durations based on our observer record. The penalty function analysis resolved the parameter set as follows: normalized mean band pass data, detection threshold triggers when the signal-to-noise ratio exceeded 17.

[28] The broadband sensor (BBB; Figure 1) recorded data intermittently from 18 June 2004 until 16 September 2005, with 238 days of partial or complete data records. Time series of hourly detection counts for all channels are shown in Figure 4. As shown in Table 1, the vertical channel detected 147,680 events, of which 54% were in the 10–20 Hz band, 46% in the 1–3 Hz passband, and <1% in the low-frequency passband (0.033–0.083; 30–15 s). The timing of maximum detections is consistent across the three channels (N, E, Z) for the 1–3 Hz passband, but not across the other passbands or between years. We also noted a 15% increase in 1–3 Hz detections from summer 2004 to summer 2005, but this increase was not recorded in the other passbands.

#### 4.4. Method Performance: Ground Truthing the Picks

[29] Minimizing the penalty function between observations and detections does not demonstrate that passive seismic observations of 1–3 Hz events actually represent calving. An independent quantifiable method of measuring

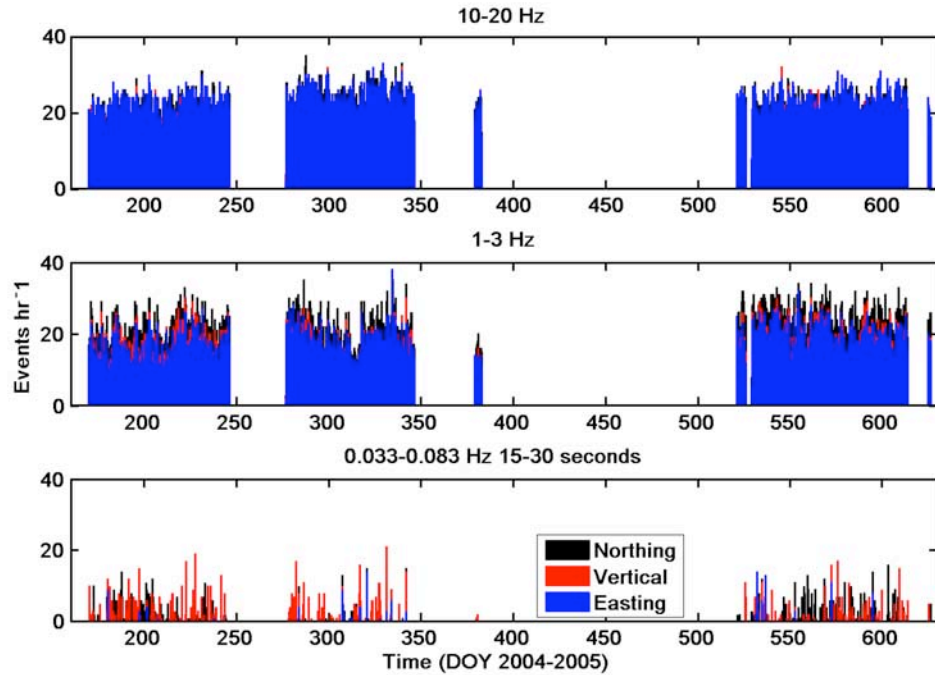


**Figure 4.** Time series plots of hourly event detections for station BBB. (a) The 10–20 Hz band, (b) the 1–3 Hz band, and (c) the 0.0833–0.033 Hz band. The passbands in Figures 4a and 4b are interpreted to represent crevassing and calving, while the low-frequency band in Figure 4c contains mostly information regarding teleseismic earthquakes. Data gaps exist where no bars are present.

calving is needed to validate whether or not 1–3 Hz detections capture and isolate the process of calving. For this task we employ time-lapse photogrammetry to quantify and compare glacier area changes between images to detection counts and durations.

[30] The rate of calving,  $U_c$ , is typically solved for as the difference between the width-averaged ice speed at the terminus,  $U_i$ , and the rate of retreat  $\frac{dL}{dt}$

$$U_c = U_i - \frac{dL}{dt} \quad (3)$$

When considering calving on short timescales, the retreat rate term dominates the difference equation, and calving rate closely tracks the rate of terminus retreat [O'Neel et al., 2003] (the opposite, nonphysical correlation occurs over long timescales, where ice speed dominates the difference [Van der Veen, 1996]). Lack of velocity data at the terminus forces the assumption that changes in terminus geometry ( $dA/dt$ ) as measured by the time-lapse camera represent a minimum bound on the rate of calving. This assumption neglects resupply ice flux into the terminus during the time between a large calving event and the next photograph.

[31] To assemble a time series of terminus area change, we follow single camera oblique photogrammetry methods described by Krimmel and Rassmussen [1986], who showed that horizontal map plane coordinates can be obtained from a single oblique photo by intersecting direction rays from the camera with a known plane. In each photo of our time lapse series, we transform image space coordinates to UTM coordinates using two GPS surveyed control points and the known position and rough

orientation of the camera. The control points allow us to solve for the intersection of the time varying plane of sea level and the glacier terminus. Next, we calculate the glacier surface area as bounded by the terminus, the margins, and a fixed reference line upstream of maximum retreat.

[32] On average, the camera took four images daily, while the seismicity time series were sampled hourly. To compare the area record with the record of event detections some smoothing and resampling is required. We use a nonparametric, kernel-smoothing filter [Bowman and Azzalini, 1997] to simultaneously resample the seismic and camera data on equal spaced intervals. Resampling at  $4 \text{ d}^{-1}$  with a 0.5 d smoothing window allows comparison over a 64 d gap-free time series, days of year 177–240 2004.

[33] Figure 5a shows the time derivative,  $\frac{dA}{dt}$ , of the glacier area time series, measured by the time-lapse camera. Event counts in the 1–3 Hz passband are shown over the same period in Figure 5b, and event durations are given in

**Table 1.** Summary of Event Detections From Broadband Station BBB<sup>a</sup>

Band	2004			2005			Total		
	HF	1–3 Hz	LF	HF	1–3 Hz	LF	HF	1–3 Hz	LF
E	60,686	37,846	98	38,677	28,189	62	99,363	66,035	160
N	61,094	51,296	624	39,163	38,988	591	100,257	90,284	1215
Z	47,638	38,697	707	31,385	28,891	362	79,023	67,588	1069

<sup>a</sup>Detections are tabulated for the 1–10 Hz high-frequency passband, the 1–3 Hz passband, and the low-frequency band of 0.033–0.083 Hz for each channel during 2004 and 2005.

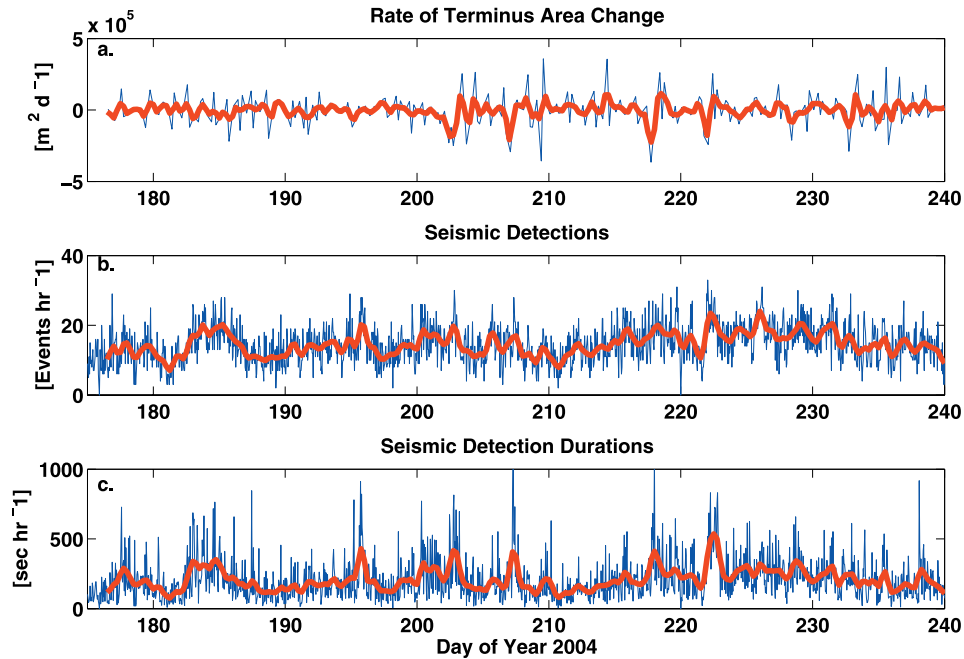


**Figure 5.** (a) Photogrammetrically derived time series of the rate of terminus area change and (b and c) 1–3 Hz hourly event counts and durations, respectively. Each plot has a red smoothed curve overlaid, which uses a 0.5 day window, sampled at 0.25 day intervals.

Figure 5c. Each series has its smooth curve overlaid. In the following sections, we use three statistical methods and hypocenter locations to compare the time series of icequake detections to geometry change in order to assess the performance of the method.

#### 4.4.1. Cross Correlation

[34] We first cross correlated the area change and seismicity data, seeking the strength and phase of any relationship between the two vectors. Besides the standard Pearson linear correlation coefficient  $r$ , we calculate Kendall's  $\tau$  and Spearman's  $\rho$  because these statistics assess monotonic correlations regardless of linearity [Helsel and Hirsch, 1992]. We calculated cross correlations with 4 lags in each direction ( $\pm 1$  day lag, 0.25 steps). P values, which give the probability that the observed correlation may occur at random, are shown for each maximum correlation. Figure 6 shows the Pearson cross correlation plot from the north–south channel of sensor BBB for event counts on each passband and durations for 1–3 Hz data.

[35] The strongest correlation occurs between 1–3 Hz event durations and geometry change ( $dA/dt$ ), using the Pearson linear correlation. At 0 lag,  $r = -0.43$  and  $p = 1 \times 10^{-12}$ , indicating a near zero probability of a random correlation, thus providing confidence that the correlation is statistically significant and that the detector is capturing calving. The sense of the correlation is negative, meaning that an increase in 1–3 Hz seismicity results in a negative change in area (i.e., calving) with no lag, as expected. We found correlation strength to depend only weakly on the channel selection, and that calculation of either rank based correlation coefficient (Kendall's  $\tau$  or Spearman's  $\rho$ ) did not improve the correlation for minimally smoothed data. However, a 25% improvement in correlation

strength (0.11) occurred when event durations replaced event counts. Smoothing over a longer window length (e.g., 0.25 d samples, 1–5 day window) also strengthens the correlation, such that  $r \sim 0.5$ –0.6. Smoothing also resulted in the Spearman rank-based coefficient exceeding the Pearson coefficient, indicative of a possible nonlinear relationship between geometry and 1–3 Hz seismicity. Correlations are very weak ( $r \sim 0.05$ ;  $p$  values  $>0.05$ ) for the other passbands at all lags.

#### 4.4.2. Power Spectral Density Comparisons

[36] Our second validation test involves direct comparison of PSDs, which give a description of data variance as a function of frequency. This comparison requires two gap-free, evenly sampled time series ( $4 \text{ d}^{-1}$ , 0.5 d window, as above) to identify any common periodic forcing between time series. In our case, similar periodic forcing would suggest that the two methods (1–3 Hz seismicity and photography) are measuring the same process.

[37] Normalized 512-point PSDs are shown in Figure 7 for the smoothed, mean-removed area change data and the 1–3 Hz north–south channel seismic detections. Analysis of the other channels produced very similar results. All three records have peaks at  $\sim 2.1$ ,  $\sim 3.5$ , and  $\sim 5.3$  days. Maximum power occurs in the  $\sim 15$ –22 day range, shifted toward longer periods for the seismic data. The long-period peaks are stronger for the seismic data than for the camera data, and may be related to fortnightly ( $\sim 2$  weeks) or monthly tidal constituents. Alternatively, increasing power at the longest periods may indicate the presence of a seasonal cycle that has not been removed from the data. Seasonal cycles in speed and geometry have been well documented at Columbia Glacier [e.g., Krimmel, 2001], and the time series of terminus area shows a substantial seasonal readvance beginning in November. This advance was also



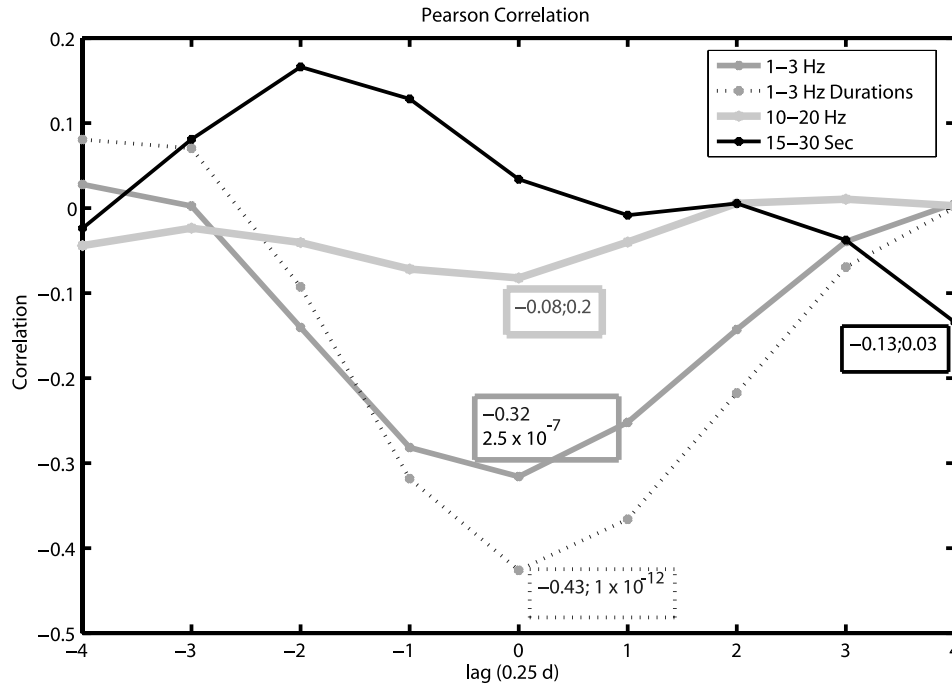


**Figure 6.** Cross correlation between north-south seismicity and area change. Four 0.25 day lags are shown in each direction, and we give p values for the maximum correlation in each case. The 1–3 Hz detection durations are shown with a dashed line, yielding the strongest correlation.

visually documented by field visits in June 2004 and February 2005. Seasonal retreat was underway again during June 2005. This long-period peak is largest in the 1–3 Hz passband, shifted toward longer periods for the 10–20 Hz passband, and only small for the low-frequency time series.

#### 4.4.3. Distribution Analyses

[38] Finally, we compare probability distributions (PDF) via quantile-quantile plots and the two-sample, Kolmogorov–Smirnov hypothesis test (KS test) [Helsel and Hirsch, 1992] to examine the hypothesis of a common statistical origin for two data vectors. Our data set is well suited to a statistical analysis of population origin due to its large size. Note that the analysis considers the absolute values of all negative area changes, which we assume are proportional to the ice volume calved. A strength of these methods is easy inclusion of all possible data, because data vectors are not required to be gap-free or the same length. These methods are nonparametric so they are appropriate for nonnormal data distributions (e.g., lognormal, Weibull).

[39] The KS test compares the cumulative probability distribution  $F(x)$  of two vectors

$$P = \max |F_1(x) - F_2(x)| \quad (4)$$

for all values. The null hypothesis claims the vectors have similar origins, and the significance level is a user specified quantity. For example, at the 95% significance level, if the cumulative distributions are more than 5% different at any location, the null hypothesis is rejected.

[40] The KS test requires scaling, which is accomplished by subtracting the mean and dividing by the standard

deviation of the data. Analysis of scaled PDFs shows that the mean values are offset, but skew and kurtosis are similar. The positively skewed seismic data has a rounder-shaped PDF and longer tails, as expected for a signal more highly contaminated by noise. KS test results confirm that the two distributions have similar statistical origins at the 95% confidence level.

[41] To avoid scaling, we graphically analyze the distribution of both data sets quantiles with qq plots. Q-q plots give a graphical representation of the quantiles of one variable plotted against the quantiles of a second variable, where a quantile defines the fraction of points below a given value. If the two data vectors come from populations with similar distributions, the points will fall along a 45° reference line. Rotational deviations indicate a multiplicative constant and DC offsets indicate an additive constant in the relation between the variables.

[42] The qq plot shown in Figure 8 suggests a similar statistical origin for area change and 1–3 Hz passband detection duration data. Data are shown for the north-south channel, and the vertical channel has a very similar appearance. The strong linear relation indicates a similar population distribution in accordance with the KS test result. Amplitude information loss is manifested as divergence between the two populations, and is evident at both tails. Upper tail divergence suggests that a single large event may have a much stronger impact on the terminus geometry than many small events. Lower tail divergence suggests that small area changes are underrepresented by the seismic data, perhaps due to isolated release of submarine bergs over short durations or the low time resolution of duration tallies. Quantile crowding at the



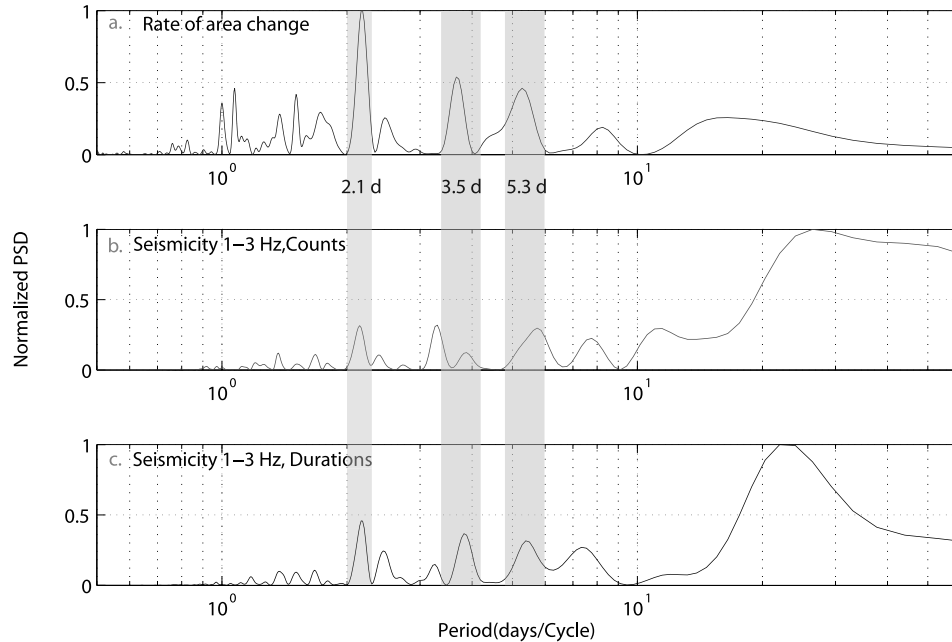


**Figure 7.** (a) Normalized PSD plots for the area change time series, (b) the time series of vertical channel event counts, and (c) the time series of vertical channel detection durations. The records show similar periodic forcing at  $\sim 2.1$ ,  $\sim 3.5$ , and  $\sim 5.3$  day periods. The strong peak appearing in the area change plot at 1 day is probably a result of multiple people digitizing photographs.

low end demonstrates that large events are much rarer than small events. The q-q plot indicates that an additive and multiplicative linear scaling relation exists between the two variables, given by  $x = 500y - 38000$ , providing a crude scaling relation between 1–3 Hz seismicity and the area change proxy for calving rate. Importantly, this linear relationship between seismicity and area change is limited only to the 1–3 Hz passband; no such pattern exists for the other analyzed passbands.

#### 4.4.4. Event Locations

[43] A decisive measure of the method's performance is demonstrated through hypocenter location. We used data from four coordinated explosions to develop a two-layer, constant velocity model consisting of a thin (0.6 km) ice layer underlain by a half-space with material properties of low-grade metamorphic rock. P wave velocities of 3.25 and 5 km/s were assigned to the ice and rock layers, respectively. We used a slightly slower value than published by *Deichmann et al.* [2000] for P wave speed in ice, due to the highly fractured and water saturated character of the ice. Because of the absence of S wave arrivals, we use only first motions to locate events, which we assume to be refracted head waves that travel vertically to the ice-rock interface and are then refracted along this interface at the P wave speed of the rock until arriving at the receiver. The largest error in this model is the upward return path, which in our case is through rock, not ice as in the model.

[44] Locations for four active source explosions were both surveyed, and then triggered using GPS, so that precise timing exists between the blasts and the sensors. Figure 9 shows the epicenter solutions for the blasts, demonstrating the first-order success of the velocity model. Hypocenter

solutions for a small subset of 1–3 Hz detections illustrate the performance of the detection method. Most hypocenters in Figure 9 are located within 2 km of the terminus at shallow depths, although an obvious seaward bias exists due to the overly simple velocity model used and difficulties identifying consistent first motions for the emergent events. Only 2 of 15 solutions indicate spurious detections were made.

## 5. Discussion

### 5.1. Method Validity

[45] We begin with a discussion of the results of statistical tests and hypocenter location analyses. Validation tests establish that 1–3 Hz detections represent the process of calving to first order, such that frequency domain detection allows both first-order identification and classification of icequakes. Herein, we refer to these detections as the calving passband. We suggest three possible causes for the unique characteristics of the calving waveforms, and then finish with an interpretation of the continuation of the retreat.

#### 5.1.1. Calving Pass Band: 1–3 Hz

[46] Our analysis indicates that detections in the 1–3 Hz passband are a valid proxy representing time changes in calving for the following four reasons. First, these detections show several nonrandom statistical relationships with changes in terminus geometry caused by calving. Second, Table 1 shows that north–south oriented detections exceed detections in the east–west and vertical directions by  $\sim 30$ – $35\%$ . This result agrees with the primarily southward flow direction near the terminus (Figure 1), and the expectation of primarily extensional, along-flow failure (versus east–west transverse

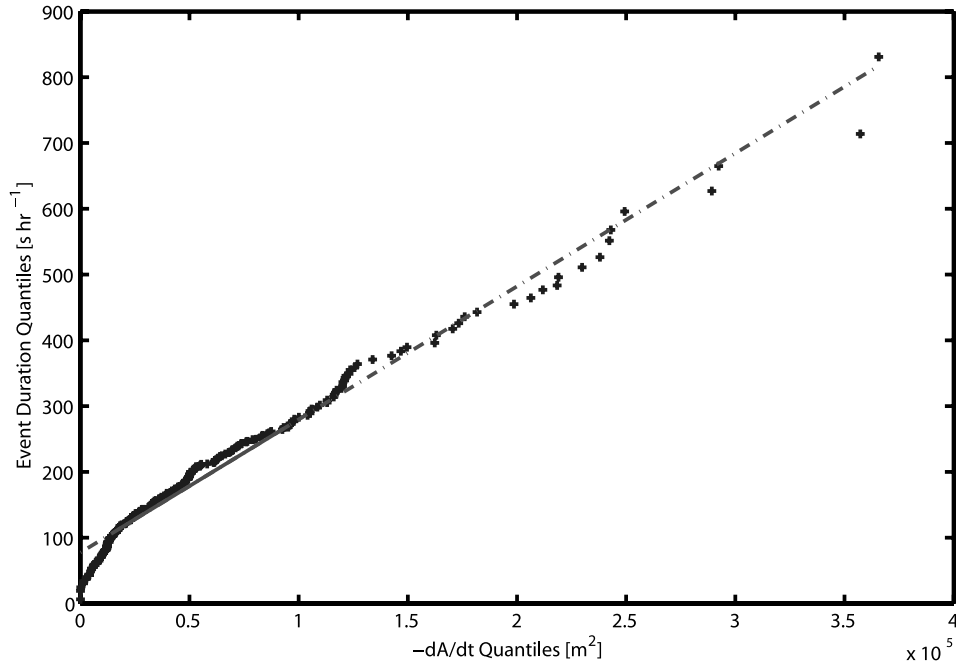


**Figure 8.** Quantile-quantile plot for negative area changes and seismic events detected in the 1–3 Hz band.

shear) producing calving events. Our third piece of evidence is that for every analyzed visual record, an associated monochromatic seismogram exists.

[47] Our final and most concrete evidence is that the majority of a subset of 1–3 Hz detection hypocenters are located near the glacier terminus, showing relatively infrequent detection triggers from other processes. Our experience performing hypocenter locations, suggests the detection record is contaminated by 10–20% events that were generated by processes other than calving. Sources may include, but are not limited to, teleseisms, local earthquakes, basal sliding, lake drainage events and hydraulic transients. Waveform characteristics for the outlying events (Figure 9) indicate that we have triggered on a local earthquake (PSD shown in Figure 3) and an internal event in the hypocenter subset presented here.

[48] The majority of contamination is likely to be from local earthquakes, which are fairly common and will have spectral overlap with calving. Teleseisms are generally characterized by lower-frequency energy, and these events likely do not contaminate the 1–3 or 10–20 Hz passbands, since energy in these frequency bands would attenuate prior to arrival. Further contamination exists from yet another type of glacier-generated seismicity, exhibiting a similar harmonic appearance to calving signals, but with epicenters upstream of the terminus (Figure 5). Other authors [e.g., *Métaxian et al.*, 2003] have also identified these events at terrestrial glaciers, and their source may be related to basal motion and hydraulics.

### 5.1.2. High-Frequency and Low-Frequency Passbands

[49] Although comparison with direct observations is not possible, detections made over the 10–20 Hz passband capture what appear to be crevassing events. However,

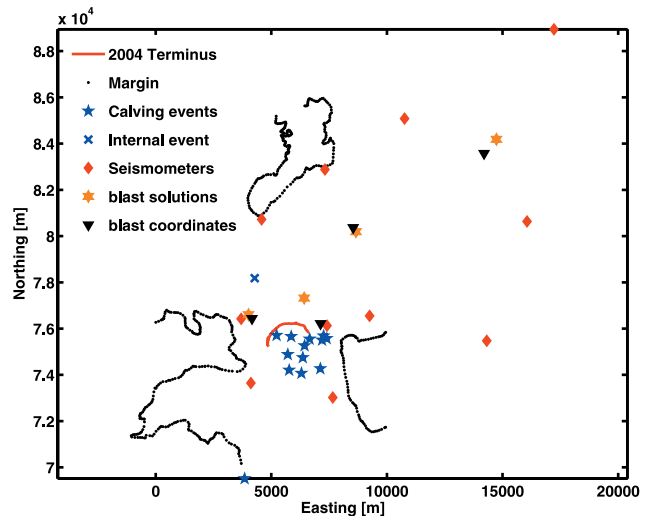


**Figure 9.** One hour of detection trigger locations, shown in map view. The lower glacier margins are depicted with dotted lines, and the 2004 terminus position is shown with a red line. GPS coordinates for blasting sites are given as triangles, and solutions using the 1-D, two-layer velocity model are shown with orange stars. Epicenters of automatically detected and observed calving events are shown as blue stars. During the time analyzed here, all observed calving events were located in the terminus region, but we triggered on a local earthquake (not shown) and an internal event, which is marked with a cross. A bias exists in our velocity model or detection methods, shifting solutions seaward of the terminus. Triggers have been manually adjusted for hypocenter solution.

detailed inspection showed that this time series is heavily contaminated by detections from short-lived pulses of high-frequency energy within longer-duration waveforms produced by calving (Figure 2b). Such events may represent fracturing during calving events and hint that multiple source processes may be important in generating icebergs. The dominant ice flow direction in the study area is to the southwest (except at the terminus, where flow is due south). Accordingly, the number of detections in both horizontal directions are similar and exceed the number of detections in the vertical direction by  $\sim 20\%$ , as expected for transverse crevasses opened by mode I tensile stresses.

[50] The low-frequency band may contain information pertaining to glaciological processes, but is predominantly composed of detections resulting from the December 2004, Great Sumatra Earthquake ( $M_0 = 9.1$ ) and associated aftershocks.

### 5.1.3. Incorporating Amplitude Information

[51] Event counting preserves no amplitude information from source data, which is essential to provide a complete description of volume change from calving. *Qamar* [1988] postulated that the peak amplitude of a calving icequake is unrelated to ice volume released, but the area of the signal coda may better quantify volume change from calving. We have calculated local magnitudes (Richter) using the maximum amplitude,  $A$ , of detected events:

$$M_L = \log_{10} A + 2.76 \log_{10} \Delta - 2.48 \quad (5)$$

where  $\Delta$  is the distance from the source in degrees, and found no correlation between  $M_L$  and observational estimates of ice volume discharge, as previously suggested by *Qamar* [1988]. We also checked to see if frequency content exhibited a relationship with ice volume release. Although approximately 35% of analyzed observer record events exhibited a significant component of energy  $< 1$  Hz, there was no systematic variation in frequency content as a function of event size or style. Events with significant power in the low-frequency spectrum resulted not only from submarine events, but also from small block failures or avalanches.

[52] However, we found we could form a rough approximation of event magnitude (ice volume) using the trigger duration for a given event as shown by both the observer record and statistical tests. Longer duration events release more ice than shorter ones, as shown most clearly in Figure 8. Inclusion of event durations strengthened all analysis methods, which suggests that the time duration of the event contains much of the amplitude information lost by simply counting events. The observer record, magnitude calculations, statistical and spectral analysis thus indicate that event duration is the primary predictor of glacier volume change from a calving event.

### 5.1.4. Future Improvements

[53] Significant room for improving the classification method exists, and we hope to implement new ideas in the near future. A more complex seismic velocity model that includes a laterally bounded, low-velocity glacier, coupled with cross correlation location methods is required to calculate robust event hypocenters, and will greatly improve

our algorithm by removing local earthquakes and internal events from the calving record. Energy calculations can be made by integrating the amplitude envelope of the triggered portions of the signal [*Qamar*, 1988], which will be a large improvement of the amplitude estimations.

## 5.2. Glaciological Interpretation

[54] The observation of similar spectral waveform content independent of ice volume discharge or maximum trace amplitude presents a strong difference between calving events and earthquakes, and poses the question of why the events possess such unique characteristics. We discuss three possible explanations for the focusing of energy in a narrow passband.

### 5.2.1. Filtering and Resonance

[55] Little is known about seismic attenuation in glacier ice, but we expect that high frequencies are rapidly attenuated. Perhaps this provides a reason for the lack of a high-frequency component in calving seismograms. Additionally, glacier ice may be acting as a high-pass filter such that low-frequency energy ( $< 1$  Hz) is filtered by the ice, and any low-frequency energy generated by calving cannot reach the seismometers. If ice has high seismic attenuation or a low seismic quality factor,  $Q$ , (as may be expected for fluid filled, faulted rock [*Métaxian et al.*, 2003; *Stein and Wysession*, 2003]) it is possible that most energy below the 1–3 Hz passband is scattered or attenuated while traveling through the glacier. Although we cannot rule this explanation out, we feel it is unlikely, because some power spectra for observed calving events contain low-frequency energy. However, the energy from such events could have reached our sensors via a raypath through the ocean and bedrock, without propagating through the ice.

[56] Rather than acting as a filter, the glacier may respond to energy inputs from mechanical failure during calving by resonating at its fundamental frequency  $f$ :

$$f \approx \frac{V_s}{2H} \quad (6)$$

Resonance frequency depends on the layer thickness,  $H$ , making this hypothesis testable using historical data. If path effects, including layer resonance, were significant, we would expect to have seen a shift in the fundamental resonance frequency due to changes in ice thickness in the near terminus region during the 25 years of retreat. Shear wave speeds,  $V_s$ , published by *Deichmann et al.* [2000] of  $2.0 \text{ km s}^{-1}$ , combined with water depth estimates taken from *Brown et al.* [1982] and collected during our study, suggest that the fundamental resonance frequency at Columbia Glacier today would be lower (because the terminus is now located in deep water the thickness in a several km neighborhood has increased since the onset of retreat) than for historical events. Tidewater glaciers all exhibit similar cliff heights ranging between 40 and 70 m [*Brown et al.*, 1982; *O'Neel et al.*, 2003], which allows ice thickness to be estimated using measured water depths under the assumption of a flat bed in the near-terminus neighborhood. The thickness at Harvard Glacier was estimated at  $\sim 110$  m thickness by *Brown et al.* [1982], and *Wolf and Davies* [1986] present PSD with peaks at



1.65 Hz. Similarly, during the 1980s at Columbia Glacier (~200 m thickness [Krimmel, 2001]), Qamar [1988] estimated the dominant frequency component of calving events at 1–2 Hz. Our measurements, using broad band sensors, reveal a higher characteristic frequency today, in contrast to resonance theory predictions of a lower-frequency fundamental mode. Additionally, we found that seismograms recorded at ranges between 0.5 and 15 km from the terminus exhibit similar spectral characteristics, thus strongly suggesting the harmonic codas are not predominantly caused by resonance. Similar to our result, Qamar concluded that the source mechanism is more important in generating the harmonic coda of calving waveforms, not spectral characteristics of the glacier.

[57] A second interpretation of concentrated calving-generated energy in the 1–3 Hz frequency range attributes a common fault size to all events, which by this hypothesis are generated by processes similar to tectonic earthquakes. If the failure process for calving bears similarities to earthquake ruptures, where frequency content scales with rupture area, then large events should be characterized by broader band energy [Stein and Wysession, 2003]. Our results show uniform spectral composition regardless of size. This suggests that large calving events do not result from a single rupture; rather they result from a series of small ruptures, for which failure occurs after a critical (but small) rupture destabilizes a large, nearly detached block of ice. Note that since standard earthquake magnitude scales are logarithmic, calving event end-members may vary only slightly on an earthquake magnitude scale. Local magnitudes calculated for both small calving events and the largest observed range from  $M_L = 1$  to 2.5, which result in a corner frequencies for small earthquakes exceeding 10 Hz, significantly different than our observations.

[58] Following this interpretation, processes leading to calving may begin by weakening the ice at significant distances upstream of the terminus. Crevasse-style ruptures may weaken the ice so that the final release of an iceberg happens from a small-area fault slip. Swarms of high-frequency events (akin to expectations of crevassing events; Figure 2), may indicate fracture during calving. Impulses like this may occur during long-duration events as single events destabilize deeper blocks of ice and cause them to fail in rapid succession. This argument strengthens the notion that duration is a good initial proxy for event magnitude, and suggests we may be able to fully quantify the energy release by integrating the time domain signal coda during events. Additionally, seismically detected calving events (1–3 Hz) and fracturing events (10–20 Hz) exhibit a linear correlation ( $r = -0.52$ ), which suggests that the two processes are not acting independently; rather there is an interaction between the two processes as ice moves toward the terminus and is eventually calved off.

[59] A third possible interpretation deviates from a tectonic-like source, and borrows from volcanoseismology theory. This idea does not eliminate our previous hypothesis, but rather provides a mechanism for some portion of calving events. Calving event seismograms can be described as monochromatic, and such seismic signals are uncommon in nature. However, earthquakes associated with some landslides and long-period (LP) volcanic events

produce similar waveforms [McNutt, 1986; Varnes and Savage, 1996; Chouet, 1996]. LP volcanic waveforms are extremely similar to those generated by calving, being characterized by emergent onsets that contain an excitation phase of high-frequency energy followed by a monochromatic 1–5 Hz coda with no clear S wave arrival [e.g., Chouet, 1996]. The source for such events is still debated, but site and/or path effects (e.g., resonance or filtering) are generally ruled out due to detection of similar waveforms at multiple stations at various distances from the source [e.g., Chouet, 1996; Métaxian et al., 2003]. A leading theory developed by Aki et al. [1977] attributes a source for LP events to slowly propagating waves in voids (cracks, conduits) within the solid medium caused by fluid pressure transients [see also St. Lawrence and Qamar, 1979; Chouet, 1996]. The nondestructive LP events attain their monochromatic form by resonating motion around constrictions or obstructions to magma flow in the voids and are very similar in space and time. LP volcanic events are much more repeatable than calving event signals (C. Rowe, personal communication, 2006), which suggests variations of the source model between the two processes. Clearly, calving is a destructive process, and this may explain the less repeatable waveforms. However, similar harmonic waveforms are generated by noncalving glaciers, although their relationship with the dynamics is unresolved [Métaxian et al., 2003; C. Larsen, personal communication, 2006]. In the glacier system, water would take the role of magma (and material properties can thus be better constrained), as the pressurized fluid aiding crack propagation. Fracturing may be initiated by hydraulic changes, producing high-frequency seismic energy, as described above. This hypothesis may be most intuitive to the large submarine events although harmonic waveforms are produced by all events.

[60] Each hypothesis has strengths and weaknesses supported by data and observations. The harmonic waveforms and observations of large floods suggests that, at least intermittently, subglacial hydraulics are actively involved in the process of iceberg calving. Repeat pulses of short-lived, high-frequency energy may indicate that pressurized water is enhancing crack propagation during prolonged events. The similar form of small subaerial events may stem from surface water generated by meteorological processes aiding in propagation of crevasse tips [Van der Veen, 1998]. This may indicate that the rupture areas are limited by maximum basal pressures such that repeated fracture propagation proceeds at small length scales until an iceberg is generated. This result suggests a percolation theory model may apply as suggested by Bahr [1995] but where water causes stress buildups in the ice. In summary, our data indicate that a combination of hypotheses two and three are involved in calving.

### 5.2.2. External Forcings

[61] A favored conceptual model for calving relates failure to exceeding a floatation threshold [e.g., Meier and Post, 1987; Van der Veen, 1996; Vieli et al., 2001; O'Neel et al., 2003, 2005]. Most discussion focuses on seasonal to secular timescales, such that the terminus position is modulated by increasing water depth or the water depth-ice thickness ratio at the terminus. Some stochastic component likely governs the smallest, most frequent events, but we

suggest that similar buoyancy arguments may govern the location and timing of large individual calving events, especially in response to rapid transients in water pressure. If water pressure transients are important for calving, we may expect some relationship between water storage and calving over daily to secular timescales.

[62] Minimum water pressure is bounded by sea level, but also modulated by the state of the subglacial hydraulic system and the ease of water throughput (e.g., bed slope). Physical conditions prohibit water storage measurements, but we can explore water input forcing by comparing the 1–3 Hz seismicity to meteorological data collected during the experiment in Valdez.

[63] We calculated PSDs for recorded temperature and precipitation data and found no direct evidence for simple forcing by either process when comparing 70 day time series. No clear evidence exists for either semidiurnal or diurnal periodicity, even given the robust data set for the statistical analysis. Although *Warren et al.* [1995] and *O'Neel et al.* [2003] found evidence for long-period tidal modulations of calving, we found no conclusive evidence for this. However, these periods require longer time series to be completely ruled out.

[64] As suggested by *Warren et al.* [1995], *O'Neel et al.* [2003], and our field observations, an internal, self-regulated forcing plays a role in calving flux variations. None of the physically motivated, external forcing processes appear to have a direct influence on calving, yet periodicities exist at  $\sim 2$ , 3, 5 and 20 days. A possible explanation involves stretching and thinning of the terminus after major calving events before reattaining critical floatation levels for large-scale calving. During this time, only minor calving events occur, and from our data it appears that this time may be  $\sim 20$  days for Columbia Glacier. This may also indicate a characteristic life span for the subglacial hydraulic system near the terminus of a fast moving outlet glacier. The weak and multiple length forcings described here are expected, because hydraulic events including rains storms, heat waves, or rapid changes in hydraulic connectivity may disrupt the natural cycle.

### 5.2.3. Framework of Rapid Retreat

[65] Our data show a 15% increase in calving between seasonally defined summer 2004 and 2005, which is in agreement with observations and knowledge of the glacier geometry and subglacial topography [*Mayo et al.*, 1979; *O'Neel et al.*, 2005]. Between 2001 and 2005, the terminus was located in the gap between Kadin Peak and the Great Nunatak (Figure 1). Prior to 2001, a significant icefall was located in this constriction, and associated steep surface slopes provided buoyancy stability and served to slow retreat rates since the late 1990s [*Krimmel*, 2001]. The slowed retreat rates have been accompanied by strong laterally convergent, concave-up downstream terminus geometries, which suggest that lateral stresses provide terminus stability while upstream thinning continues. Thinning and upstream drawdown have continued or accelerated, reducing the glacier width by  $\sim 50\%$  and changing the icefall into a very flat, dynamically sensitive region of the glacier.

[66] During winter 2004 and 2005, and possibly before, large ( $\sim 0.5 \times 0.5$  km) embayments formed at the glacier terminus west margin. These excursions suggest that stability is being lost, and that retreat from the constriction is

imminent. Most recent observations in September 2006 suggest that this has occurred. Higher rates of calving are likely in the near future, as retreat from the gap will increase the terminus width while remaining in deep (or deeper) water, sustaining large buoyancy forces near the terminus. This is especially true because initial retreat from the constriction will cause a nonlinear increase in terminus width as it enters the confluence of the West and Main Branches of the glacier. The width of the calving cliff will increase from approximately 2 km to 7–10 km with only  $\sim 2$  km of further retreat, and over a majority of this terminus, water depths will remain deep ( $\sim 500$  m). No known major obstructions to retreat exist until the location where the bed rises above sea level (km 36) and the glacier surface is relatively flat up to this location. However, there are suggestions of basal bumps  $\sim 4$  km upstream from the terminus, which may retard the retreat rate. Thus we expect that upon retreat from the constriction, retreat rates will increase dramatically.

## 6. Conclusions

[67] Results from an eleven sensor array deployed around lower Columbia Glacier reveal interesting aspects of the mechanical processes occurring during iceberg calving. Although seismometers record ground motion from any source, we used a broad band seismometer to definitively show that all calving events produce seismic energy with a narrow-band spectral signature. Power is focused between 1 and 3 Hz for all observed events. This spectral signature is distinct from other glacier generated seismic signals and local earthquakes.

[68] Frequency domain detection methods were developed to automatically detect calving events. Four validation methods show the effectiveness of our detection methods at finding and isolating calving events from the total seismicity. Our validation tests also show that Earthquake magnitudes do not capture the size of a calving event, but a first-order estimate of ice discharge is attainable via event durations.

[69] We investigated the origin of the unique waveforms generated by calving. Their monochromatic form does not appear to be solely an effect of resonance of the glacier, but may be related to a common fault size for all events or indicative of direct involvement of hydraulic processes. Our analyses provide no evidence for semidiurnal (tidal) or diurnal forcing (melt) for iceberg calving. A self regulating cycle of thinning to a critical floatation level may be largely responsible for the large infrequent events that dominate observed changes in terminus geometry.

[70] Our results show that passive seismic observations yield a direct measurement technique for mechanical calving at Columbia Glacier that can be widely applied to glaciers in variable environments.

[71] **Acknowledgments.** This project was funded by NSF OPP 0327345. We express thanks to the IRIS/PASSCAL for providing seismic equipment, UNAVCO for supporting all GPS efforts, and VECO for logistical support. Thanks to Tim Parker, Jake Walter, and Ellie Boyce for help with field work and Thomas Hart for active source seismic support. Martin Truffer made the single-camera photogrammetry code available for use. This project would not have been possible without the skilled piloting of Jim Harvey and Jan Gunderson. Doug Benn, Tavi Murray, and an anonymous reviewer helped greatly to improve the manuscript.

## References

- Aki, K., M. Fehler, and S. Das (1977), Source mechanism of volcanic tremor: Fluid-driven crack models and their implication to the 1963 Kilauea eruption, *J. Volcanol. Geotherm. Res.*, **2**, 259–287.
- Anandakrishnan, S., and C. R. Bentley (1993), Microearthquakes beneath ice streams B & C, West Antarctica: Observations and implication, *J. Glaciol.*, **39**, 455–462.
- Arendt, A., K. Echelmeyer, W. Harrison, C. Lingle, S. Zirnheld, V. Valentine, B. Ritchie, and M. Druckenmiller (2006), Updated estimates of glacier volume changes in the western Chugach Mountains, Alaska, and a comparison of regional extrapolation methods, *J. Geophys. Res.*, **111**, F03019, doi:10.1029/2005JF000436.
- Bahr, D. (1995), Simulating iceberg calving with a percolation model, *J. Geophys. Res.*, **100**, 6225–6232.
- Bowman, A. W., and A. Azzalini (1997), *Applied Smoothing Techniques for Data Analysis*, Oxford Univ. Press, New York.
- Brown, C. S., M. F. Meier, and A. Post (1982), Calving speed of Alaska tidewater glaciers, with application to Columbia Glacier, *U.S. Geol. Surv. Prof. Pap.*, **1258-G**.
- Calkin, P. E., G. C. Wiles, and D. J. Barclay (2001), Holocene coastal glaciation of Alaska, *Quat. Sci. Rev.*, **20**, 449–461.
- Chouet, B. A. (1996), Long-period volcano seismology: Its source and use in eruption forecasting, *Nature*, **380**, 309–316.
- Deichmann, N., J. Ansgor, F. Scherbaum, A. Aschwanden, F. Bernardi, and G. H. Gudmundsson (2000), Evidence for deep icequakes in an alpine glacier, *Ann. Glaciol.*, **31**, 85–90.
- Dyrgerov, M. B., and G. J. McCabe (2006), Associations between accelerated glacier mass wastage and increased summer temperature in coastal regions, *Arct. Antarct. Alp. Res.*, **38**(2), 190–197.
- Ekström, G., M. Nettles, and G. Albers (2003), Glacial earthquakes, *Science*, **302**, 622–624.
- Ekström, G., M. Nettles, and V. Tsai (2006), Seasonality and increasing frequency of Greenland glacial earthquakes, *Science*, **311**, 1756–1758.
- Fischer, M. P., and R. D. Powell (1998), A simple model of push-moraine banks on the calving and stability of glacial tidewater termini, *J. Glaciol.*, **44**(146), 31–42.
- Harris, F. J. (1978), On the use of windows for harmonic analysis with the discrete Fourier transform, *Proc. IEEE*, **66**(1), 51–83.
- Helsel, D. R., and R. M. Hirsch (1992), *Statistical Methods in Water Resources*, 522 pp., Elsevier, New York.
- Howat, I. M., I. Joughin, and S. Tulaczyk (2005), Rapid retreat and acceleration of Helheim Glacier, east Greenland, *Geophys. Res. Lett.*, **32**, L22502, doi:10.1029/2005GL024737.
- Joughin, I. (2006), Greenland rumbles louder as glaciers accelerate, *Science*, **311**, 1719–1720.
- Krabill, W., et al. (2004), Greenland Ice Sheet: Increased coastal thinning, *Geophys. Res. Lett.*, **31**, L24402, doi:10.1029/2004GL021533.
- Krimmel, R. M. (2001), Photogrammetric data set, 1957–2000, and bathymetric measurements for Columbia Glacier, Alaska, *U.S. Geol. Surv. Water Resour. Invest. Rep.*, **01-4089**, 40 pp.
- Krimmel, R. M., and L. A. Rassmussen (1986), Using sequential photography to estimate ice velocity at the terminus of Columbia Glacier, Alaska, *Ann. Glaciol.*, **8**, 117–123.
- Lee, W. H. K., and S. W. Stewart (1981), *Principles and Applications of Microearthquake Networks*, Elsevier, New York.
- Mayo, L. R., D. C. Trabant, R. March, and W. Haeberli (1979), Columbia Glacier stake location, mass balance, glacier surface altitude and ice radar data 1978 measurement year, *U.S. Geol. Surv. Open File Rep.*, **79-1168**.
- McNutt, S. R. (1986), Observations and analysis of B-type earthquakes, explosions, and volcanic tremor at Pavlof Volcano, Alaska, *Bull. Seismol. Soc. Am.*, **76**, 153–175.
- Meier, M. F., and A. Post (1987), Fast tidewater glaciers, *J. Geophys. Res.*, **92**, 9051–9058.
- Métaxian, J. P., S. Araujo, M. Mora, and P. Lesage (2003), Seismicity related to the glacier of Cotopaxi Volcano, Ecuador, *Geophys. Res. Lett.*, **30**(9), 1483, doi:10.1029/2002GL016773.
- Motyka, R. J. (1997), Deep-water calving at LeConte Glacier, southeast Alaska, in *Calving Glaciers: Report of a Workshop, February 28–March 2, 1997*, edited by C. J. Van der Veen, *BPRC Rep. 15*, pp. 115–118, Byrd Polar Res. Cent., Ohio State Univ., Columbus.
- Motyka, R. J., L. Hunter, K. Echelmeyer, and C. Connor (2003), Submarine melting at the terminus of a temperate tidewater glacier, LeConte Glacier, Alaska, U.S.A., *Ann. Glaciol.*, **36**, 57–65.
- Neave, K. G., and J. C. Savage (1970), Icequakes on the Athabasca Glacier, *J. Geophys. Res.*, **75**, 1351–1362.
- O'Neil, S., K. A. Echelmeyer, and R. J. Motyka (2003), Short-term variations in calving of a tidewater glacier: LeConte Glacier, Alaska, *J. Glaciol.*, **49**, 587–598.
- O'Neil, S., W. T. Pfeffer, R. Krimmel, and M. F. Meier (2005), Evolving force balance at Columbia Glacier, Alaska, during its rapid retreat, *J. Geophys. Res.*, **110**, F03012, doi:10.1029/2005JF000292.
- Qamar, A. (1988), Calving icebergs: A source of low-frequency seismic signals from Columbia Glacier, Alaska, *J. Geophys. Res.*, **93**, 6615–6623.
- Rignot, E., and P. Kanagaratnam (2006), Changes in the velocity structure of the Greenland Ice Sheet, *Science*, **311**, 986–990.
- Stein, S., and M. Wysession (2003), *An Introduction to Seismology, Earthquakes, and Earth Structure*, Blackwell, Malden, Mass.
- St. Lawrence, W., and A. Qamar (1979), Hydraulic transients: A seismic source in volcanoes and glaciers, *Science*, **203**, 654–656.
- Van der Veen, C. J. (1996), Tidewater calving, *J. Glaciol.*, **42**, 375–385.
- Van der Veen, C. J. (1998), Fracture mechanics approach to penetration of surface crevasses on glaciers, *Cold Reg. Sci. Technol.*, **27**, 31–47.
- Van Wormer, D., and E. Berg (1973), Seismic evidence for glacier motion, *J. Glaciol.*, **12**, 259–265.
- Varnes, D. J., and W. Z. Savage (1996), The Slumgullion earth flow: A large-scale natural laboratory, *U.S. Geol. Surv. Bull.*, **2130**, 95 pp.
- Viel, A., M. Funk, and H. Blatter (2001), Flow dynamics of tidewater glaciers: A numerical modeling approach, *J. Glaciol.*, **47**, 595–606.
- Warren, C. R., N. F. Glasser, S. Harrison, V. Winchester, A. R. Kerr, and A. Rivera (1995), Characteristics of tide-water calving at Glacier San Rafael, Chile, *J. Glaciol.*, **41**, 273–289.
- Weaver, C. S., and S. D. Malone (1979), Seismic evidence for discrete glacier motion at the rock-ice interface, *J. Glaciol.*, **23**, 171–184.
- Wolf, L. W., and J. N. Davies (1986), Glacier-generated earthquakes from Prince William Sound, Alaska, *Bull. Seismol. Soc. Am.*, **76**, 367–379.

H. P. Marshall, D. E. McNamara, S. O'Neil, and W. T. Pfeffer, Institute of Arctic and Alpine Research, University of Colorado, 1560 30th Street, Campus Box 450, Boulder, CO 80309-0450, USA. (shad@colorado.edu)